A New Sequence Domain EMT-Level Multi-Input Multi-Output Frequency Scanning Method for Inverter Based Resources

Lei Meng, Ulas Karaagac, Keijo Jacobs

***Abstract*-- The impedance-based stability analysis (IBSA) is an effective method for identifying instability issues caused by grid-connected inverter-based resources (IBRs). The electromagnetic transient (EMT)-level positive sequence and dq-frame frequency scanning methods (p-scan and dq-scan, respectively) are widely used to measure the impedance models of IBRs. The p-scan is easier to implement but has inaccuracy issue because it ignores the mirror frequency effect (MFE). The dq-scan is accurate but cannot differentiate the resonance and mirror frequencies. This paper proposes a new EMT-level coupled sequence domain (CSD) multi-input multi-output (MIMO) frequency scanning method (CSD-scan) in stationary frame. The CSD-scan usage in IBSA 1) accounts for the MFE; 2) differentiates the resonance and mirror frequencies; 3) requires no coordinates transformation for perturbation and measurement signals; 4) significantly reduces computational burden compared to the existing coupled sequence scanning method. This paper also demonstrates the impedance transformation relation between dq-domain and stationary frame CSD. The accuracy and time efficiency of the proposed CSD-scan is validated in both IBSA and EMT simulations on a weak grid test case incorporating full-size converter (FSC)-based wind park (WP) by comparing with p- and dq-scans.**

***Keywords*: CSD-scan, EMT-level frequency scanning, impedance-based stability analysis, mirror frequency effect.**

I. Introduction

THE wind and solar energy as well as the size of their generation units have dramatically increased in recent years . These renewables are normally connected to electrical grids through power electronic converters, and they are referred to as inverter-based resources (IBRs). Real-life incidents have shown that the controllers of IBRs can adversely interact with the series compensated or weakly tied AC grids in the sub-synchronous frequency range [1]. Therefore, there has been a growing interest in developing effective SSI identification tools and mitigation methods [2]-[15].

Various methods have been used such as the state-space-based assessment (SSA) [3]-[5], [16], impedance-based stability analysis (IBSA) [5]-[8], [17], and electromagnetic transient (EMT) simulation-based assessment [18]. SSA is an effective method for interpreting the instability mechanism with the dominant eigenvalues of critical modes [16]. However, due to simplifications in the process of system linearization, state-space models might not represent the original system in full detail [3]-[5], [16]. Moreover, it is not practical to apply the SSA to large-scale power systems [2].

Recently, IBSA has gained popularity due to its ease of implementation and suitability for use in large-scale power systems [2]. Highly accurate frequency dependent impedances/admittances of IBRs can be extracted from EMT-level simulations instead of simplified analytical models [5], [7]-[10]. This method also allows extracting impedance characteristics of manufacturer-specific models (i.e., black-box models), hence it is widely used in engineering practices [2], [7]-[10]. The time domain EMT simulation-based assessment is typically performed for representative scenarios to validate either the SSA or IBSA results.

The EMT-level positive-negative sequence frequency scanning (p, n-scan) was developed to obtain the single-input single-output (SISO) positive and negative sequence impedances of IBRs for IBSA. As the system is generally safe from the negative sequence interactions, usually only the positive sequence SISO IBSA is performed to identify the potential IBR instabilities. Due to its simplicity, the IBSA using the p-scan is widely adopted by transmission system operators (TSOs) [2], [5], [7], [8].

However, the accuracy of sequence SISO IBSA has been recently questioned as it ignores the mirror frequency effect (MFE) in IBRs [11], [12]. The MFE is generated by the asymmetry of the IBR due to the phase locked loop (PLL) and different outer-loop control strategies in d- and q- axis [11], [13]. In [9], [10], the dq reference frame (dq-frame) multi-input multi-output (MIMO) admittance model is developed to account for the MFE in IBSA using the EMT-level dq-frame frequency scanning (dq-scan) method. However, the obtained dq MIMO admittance model cannot distinguish between resonance and mirror frequencies (f_r and f_m, respectively) as it incorporates both the super-synchronous positive and sub-synchronous negative sequence admittances. Identifying f_r and f_m requires additional information such as phase domain voltage/current frequency spectrum analysis based on EMT simulations of the system under study.

The MFE can also be captured in the MIMO impedances in the coupled sequence domain (CSD), in either the rotating

This work was supported by the Hong Kong Research Grant Council for the Research Project under Grant 25223118.

L. Meng and U. Karaagac are with the Department of Electrical Engineering, Hong Kong Polytechnic University, Hung Hom, Kowloon, Hong Kong (e-mail of corresponding author: ulas.karaagac@polyu.edu.hk).

K. Jacobs is with the Department of Electrical Engineering, Polytechnique Montréal, Montreal, QC, Canada.

Paper submitted to the International Conference on Power Systems Transients (IPST2023) in Thessaloniki, Greece, June 12-15, 2023.

synchronous frame [13] or stationary frame (SF) [14], [15], [20]. In [15], a time domain frequency scanning method was developed in αβ-frame to extract the mirror frequency couplings. However, its effectiveness in IBSA was not tested. Moreover, the computational burden of the method in [15] for the frequency range from 1 Hz to twice the fundamental frequency is about twice of the dq-scan.

This paper proposes a new EMT-level CSD MIMO frequency scanning method (CSD-scan) in SF to obtain the CSD impedance and its use in IBSA. The proposed method captures cross couplings between the positive and negative sequence admittances, providing improved accuracy compared to the p-scan method. The method operates directly in the phase domain, eliminating the need for coordinate transformation of perturbation and measurement signals, or measured CSD impedances, making it more straightforward to implement than the dq-scan method. Additionally, the obtained CSD impedance differentiate the resonance and mirror frequencies, addressing a limitation of the dq-scan method. The computational burden of the proposed CSD-scan method is half of that of the existing method presented in [15] in 1 Hz to twice the fundamental frequency. Its effectiveness is demonstrated on a weakly-tied full-size converter (FSC)-based wind park (WP) benchmark and validated through EMT simulations.

This paper is organized as follows. Section II introduces the test case. Section III introduces the procedure and technical details of the CSD-scan method. In Section IV, characteristics and transformation relations of the obtained CSD impedance of the IBR (i.e., the FSC-based WP) are discussed. The accuracy of CSD IBSA is validated by comparing with the sequence SISO and dq IBSA, and computational burden of the CSD-scan is compared with dq-scan method. Section V concludes the paper.

II. System Under Study

The system used for testing the proposed CSD-scan method is shown in Fig. 1. An FSC-based WP is connected to a 500 kV large-scale system ($\mathbf{V_{net}}$) through two parallel equivalent impedances ($\mathbf{Z_1}$ and $\mathbf{Z_2}$). The system is initially stable, and at 5 s a contingency occurs and $\mathbf{Z_2}$ is disconnected by opening the switch, leaving the WP radially connected to $\mathbf{Z_1}$. The weak grid issue occurs as a result of a decrease in the system's total short circuit ratio (SCR) from 3.87 to 1.02.

This paper adopts the wind turbine (WT) model developed in [19]. Important system and control parameters are listed in Table I. It should be noted that, for demonstration purposes, the inner-loop control parameters of the grid side converter (GSC) of the FSC-based WT (i.e., the rise time of i_d and i_q) are modified to generate a higher asymmetry in FSC dynamics.

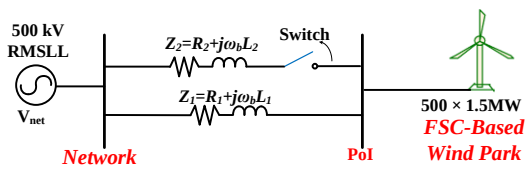

Fig. 1. The system under study.

Table I
Parameters of The Wind Power Systems

Item	Param./ Expr.	Value
System frequency	f_b	60 Hz
Power base	S_{base}	833.5 MVA
Power level	P_{PoI}	0.90 p.u.
Reactive power	Q_{PoI}	0 p.u.
Voltage base	V_{base}	500 kV RMSLL
Z_2	$\lvert R_2+j\omega_bL_2\rvert$	0.39 p.u.
	R_2/ω_bL_2	0.1
Z_1	$\lvert R_1+j\omega_bL_1\rvert$	1.02 p.u.
	R_1/ω_bL_1	0.1
WT Nominal voltage	V_{WT}	575 V RMSLL
FSC GSC inner loop rise time	$t_{r\text{-}GSC}$	i_d: 4 ms; i_q: 7 ms
GSC dc-voltage time constant	t_{dc}	150 ms

Note: $\omega_b = 2\pi f_b$: angular fundamental frequency.

In the time domain EMT simulation, growing oscillations arise immediately after the disconnection of $\mathbf{Z_2}$, as shown in Fig. 2. A 108 Hz dominant oscillation and a 12 Hz mirror frequency oscillation are found in the output voltage and current frequency spectra of the FSC-based WT (see Fig. 3).

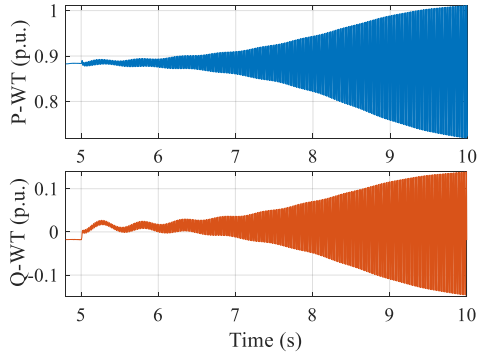

Fig. 2. Output active and reactive power of FSC-based WT.

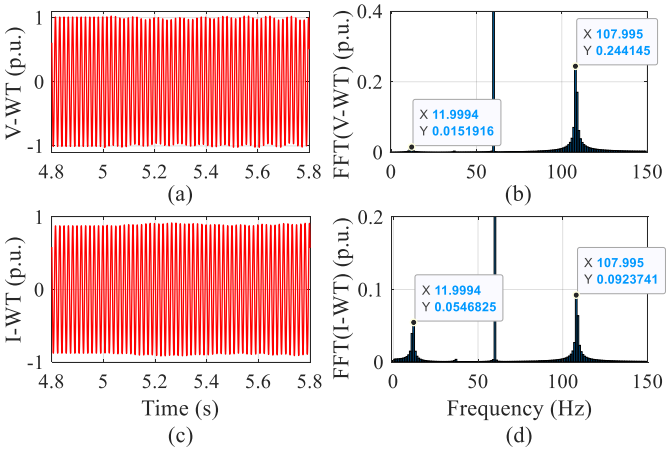

Fig. 3. Instable oscillations at t = 5 s: (a) Output voltage (phase-a) and its (b) frequency spectrum (8-9 s), (c) output current (phase-a) and its (d) frequency spectrum (8-9 s) of the FSC-based WT.

III. Measurements of the MIMO CSD-Impedance

The IBR integrated system is typically separated into the grid and IBR subsystems from the point of interconnection (PoI) (see Fig. 1), and the MIMO CSD impedance of each subsystem is measured separately.

A. EMT-Level CSD-Scan Procedures for IBR

1) CSD-Scan Procedure

The schematic diagram for the EMT-level frequency scanning method of the IBR-side CSD-scan is shown in Fig. 4. The grid side subsystem is represented by its Thevenin equivalent, a voltage source $(\mathbf{v_0})$ in series with the impedance of the grid side subsystem $(\mathbf{Z_{sys}})$ [8]. $\mathbf{v_0}$ and $\mathbf{Z_{sys}}$ maintain the same stable operating points of the CSD-scan and the original EMT-simulation systems. In the test system, $\mathbf{Z_{sys}} = Z_1 // Z_2$, and $\mathbf{v_0}$ can be adjusted to achieve the desired steady-state operating point at the POI.

EMT-type simulation programs have specific initialization methods for the IBR models and a certain time is needed for initialization transients to vanish. To improve the simulation efficiency, a steady state snapshot of the system is taken during the first simulation and loaded for each subsequent scanning simulation. The CSD-scan procedures are given as follows:

a) **Perturbation:** The balanced three-phase sinusoidal perturbations $\mathbf{v_{p\text{-}abc}}(f_i, t)$ with appropriate amplitude (0.01 p.u. in this work) are superposed on the steady state voltage $\mathbf{v_{0\text{-}abc}}(t)$.

b) **Measurement:** The three-phase currents $(\mathbf{i_{mea\text{-}abc}}(t))$ are measured at the point of injection. The discrete Fourier transform (DFT) analysis is applied to extract the frequency spectrum of the current measurements at f_i and $|f_i - 2f_b|$. It should be noted that the positive sequence responses at f_i and negative sequence responses at $f_i - 2f_b$ constitute the mirror frequency couplings [11], [13].

c) **Impedance Calculation:** Two components of the CSD admittance of the IBR $(\mathbf{Y_{IBR}^{CSD}}(f_i))$ can be calculated from the perturbation of the positive sequence:

$$Y_{IBR}^{p,p}(f_i) = \frac{\left|I_p^p(f_i)\right|}{\left|V^p(f_i)\right|}\left(\angle I_p^p(f_i) - \angle V^p(f_i)\right)$$
$$Y_{IBR}^{n,p}(f_i) = \frac{\left|I_n^p(f_i - 2f_b)\right|}{\left|V^p(f_i)\right|}\left(\angle I_n^p(f_i - 2f_b) - \angle V^p(f_i)\right) \quad (1)$$

where $|\bullet|$ and $\angle$ indicate magnitude and phase angle of a phasor, respectively; V and I are the phasors of perturbation and measurement signals, respectively;. superscripts of V and I indicate the sequence (p -positive, n -negative) of perturbation, and the subscripts of I indicate the sequence of the measured current.

d) Analog to step a) - c), perturbing the system with $\mathbf{v_{p\text{-}abc}}(f_i - 2f_b, t)$ yields the other two components of $\mathbf{Y_{IBR}^{CSD}}(f_i)$:

$$Y_{IBR}^{p,n}(f_i) = \frac{\left|I_p^n(f_i)\right|}{\left|V^n(f_i - 2f_b)\right|}\left(\angle I_p^n(f_i) - \angle V^n(f_i - 2f_b)\right)$$
$$Y_{IBR}^{n,n}(f_i) = \frac{\left|I_n^n(f_i - 2f_b)\right|}{\left|V^n(f_i - 2f_b)\right|}\left(\angle I_n^n(f_i - 2f_b) - \angle V^n(f_i - 2f_b)\right) \quad (2)$$

e) **Convergence:** In the presence of noise and harmonics, the calculated admittance parameters exhibit variations over time. Convergence criteria are set to ensure that the variations in magnitude and phase angle of each component are negligible. The convergence criteria for $Y_{IBR}^{pn}(f_i)$ is:

$$\left|\frac{d\left|Y_{IBR}^{j,k}(f_i)\right|}{\left|Y_{IBR}^{j,k}(f_i)\right|}\right| < tol \;\&\; \left|\frac{d\,Ang\left(Y_{IBR}^{j,k}(f_i)\right)}{Ang\left(Y_{IBR}^{j,k}(f_i)\right)}\right| < tol \quad (3)$$

where $j,k \in \{p, n\}$; tol is the convergence tolerance. Once the convergence criteria are met, the CSD-scan tool stops the EMT simulation, records the admittances for post-processing, and repeats the simulation for the next frequency.

f) **Processing:** The equivalent system impedance should be removed from the measured impedance to yield the IBR impedance:

$$\mathbf{Z_{IBR}^{CSD}}(f_i) = \left(\mathbf{Y_{IBR}^{CSD}}(f_i)\right)^{-1} - diag\left(\left[Z_{sys}(f_i) \quad Z_{sys}(f_i - 2f_b)\right]\right) \quad (4)$$

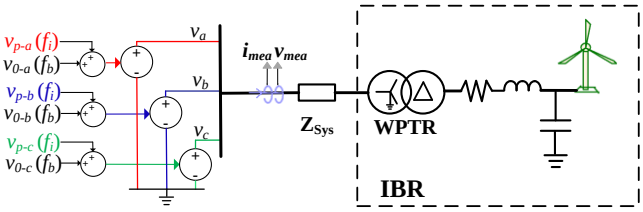

Fig. 4. Schematic diagram of voltage perturbation based CSD-scan method.

2) CSD-Scan Technical Details

a) The amplitude of perturbation signals has an important impact on both the accuracy and convergence speed of the EMT-level frequency scanning. It should be large enough to overcome the noise, but small enough not to activate any non-linearity, such as transient functions or converter saturation [7], [8], [10]. In this paper, the perturbation amplitude is 0.01 p.u. which is commonly used. Typically, increasing the perturbation amplitude (at most 0.1 p.u.) may increase the accuracy and convergence speed.

b) The rectangular window function is used in the DFT analysis to eliminate the spectral leakage. The length of the DFT window should span an integer number of the cycles of fundamental, perturbation, and coupling frequencies [20]. Variable DFT window size (e.g., the length of window is adjusted with the variation of perturbation signal frequency) can be used to increase the convergence speed but it may fail to converge at specific frequencies. To obtain reliable results, a constant window size, of at least 1 s, is recommended. This paper uses DFT window size of 1 s, and in some utilizations, 5 s or even 10 s DFT window size is used to increase the scanning accuracy.

c) The admittance variation rate might be extremely small for particular frequencies, and the convergence detection program might stop the simulation before it comes to a steady state. A forced running time can be set to eliminate the issue. In this paper, a 6 s forced running time (counting from the start of DFT work) is used.

d) In the frequency range 1 Hz to $2f_b - 1$ Hz, the negative

sequence sinusoidal signal at $f_i - 2f_b$ is equivalent to the positive sequence signal at $2f_b - f_i$, and the impedance/ admittance of IBR at $f_i - 2f_b$ in negative sequence is equivalent to the conjugate of the measured positive sequence impedance at $2f_b - f_i$. Therefore, the components of $\mathbf{Y}_{\mathbf{IBR}}^{\mathbf{CSD}}(f_i)$, i.e., $Y_{IBR}^{p,n}(f_i)$ and $Y_{IBR}^{n,n}(f_i)$, can be obtained using:

$$Y_{IBR}^{p,n}(f_i) = Y_{IBR}^{n,p*}(2f_b - f_i), \quad Y_{IBR}^{n,n}(f_i) = Y_{IBR}^{p,p*}(2f_b - f_i) \quad (5)$$

where * is the complex conjugate operator. It can be seen from (5) that one time of perturbating can determine two admittance components at both the perturbation (f_i) and mirror $(2f_b - f_i)$ frequencies. Therefore, only one set of perturbations from 1 Hz to $2f_b - 1$Hz is required to obtain the CSD admittance in the same frequency range.

e) Although $Y_{IBR}^{p,n}(f_i)$, $Y_{IBR}^{n,p}(f_i)$, and $Y_{IBR}^{n,n}(f_i)$ are represented as components of the IBR CSD admittance at f_i, they don't indicate the dynamics/ impedance characteristics of the IBR at f_i. This kind of representation is used for the convenience of utilization. Details of impedance characteristics will be discussed in the next section.

B. Measurement of Grid Side CSD Impedance

As the grid side subsystem in Fig. 1 is a sequence decoupled impedance model, it can be represented analytically as:

$$\mathbf{Z}_{\mathbf{Grid}}^{\mathbf{CSD}}(f_i) = \begin{bmatrix} Z_1(f_i) & \\ & Z_1(f_i - 2f_b) \end{bmatrix} \quad (6)$$

For a general electrical power grid, the phasor-solution-based frequency scanning method can be used to obtain its sequence SISO impedances because it is impractical to conduct the EMT-level frequency scanning to large-scale power systems [21]. The grid itself may also contain IBRs, they should be represented by pre-determined impedance tables acquired through EMT-level p-scan procedures [2].

C. CSD Impedance-Based Stability Analysis Method

The generalized Nyquist criterion (GNC) is widely used for multivariable IBSA [22]. The CSD impedance/admittance-based open-loop transfer function of the whole system is defined as:

$$\mathbf{L}^{\mathbf{CSD}}(f) = \mathbf{Z}_{\mathbf{Grid}}^{\mathbf{CSD}}(f)\mathbf{Y}_{\mathbf{IBR}}^{\mathbf{CSD}}(f) \quad (7)$$

The system is stable if the eigenvalue loci of $\mathbf{L}^{\mathbf{CSD}}(f)$ do not encircle (-1, j0) under the following assumptions [23]: i) the grid side system is stable without IBR, and ii) the IBR is stable when connected to an ideal voltage source.

IV. Validation of the CSD-Scan

In this section, the effectiveness of the proposed CSD-scan method is validated via comparison with dq- and p-scan methods and IBSA.

A. Characteristics of the obtained CSD-Impedances

The proposed CSD-scan method is applied to the FSC-based WP in Fig. 1. The obtained CSD admittances in the frequency range of 1 Hz to 119 Hz are shown in Fig. 5 The characteristic confirms that the CSD admittances meet (5).

It should be noted that $Y_{IBR}^{np}(f_i)$ represents the negative sequence current response at $f_i - 2f_b$ to a positive sequence voltage perturbation at f_i; $Y_{IBR}^{pn}(f_i)$ represents the positive sequence current response at f_i to a negative sequence voltage perturbation at $f_i - 2f_b$.

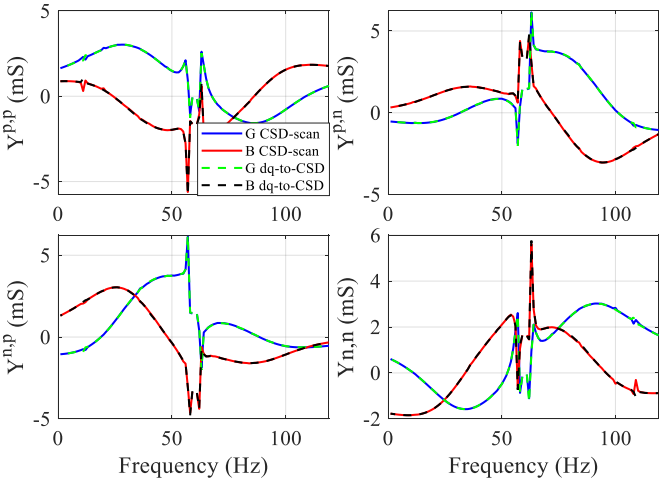

Fig. 5. CSD admittances of the FSC-based WP in SF. Solid lines: admittances obtained from the CSD-scan method; dash lines: transformed from dq-admittances. G, and B are real and imaginary parts of each admittance component, respectively.

B. Impedance Transformation Between dq- and Stationary-Frames

The CSD-impedance obtained from the CSD-scan method is intrinsically equivalent to the dq-impedance obtained from the dq-scan method, and they can be transformed into each other. The dq-impedance of IBR $(\mathbf{Z}_{\mathbf{IBR}}^{\mathbf{dq}}(f_i))$ can be first transformed into a synchronous rotating-frame (SRF) CSD model $(\mathbf{Z}_{\mathbf{IBR}}^{\mathbf{r\text{-}CSD}}(f_i))$ by the linear complex transformation [13]:

$$\begin{aligned} \mathbf{Z}_{\mathbf{IBR}}^{\mathbf{r\text{-}pn}}(f_i) &= \begin{bmatrix} Z_{IBR}^{r-p,p}(f_i) & Z_{IBR}^{r-p,n}(f_i) \\ Z_{IBR}^{r-n,p}(f_i) & Z_{IBR}^{r-n,n}(f_i) \end{bmatrix} \\ &= \mathbf{C}\mathbf{Z}_{\mathbf{IBR}}^{\mathbf{dq}}(f_i)\mathbf{C}^{-1} = \frac{1}{2}\begin{bmatrix} 1 & j \\ 1 & -j \end{bmatrix}\mathbf{Z}_{\mathbf{IBR}}^{\mathbf{dq}}(f_i)\begin{bmatrix} 1 & 1 \\ -j & j \end{bmatrix} \end{aligned} \quad (8)$$

Then $\mathbf{Z}_{\mathbf{IBR}}^{\mathbf{r\text{-}CSD}}(f_i)$ is transferred into SF through frequency shift:

$$\begin{aligned} \mathbf{Z}_{\mathbf{IBR}}^{\mathbf{CSD}}(f_b + f_i) &= \begin{bmatrix} Z_{IBR}^{r-p,p}(f_i) & Z_{IBR}^{r-p,n}(f_i) \\ Z_{IBR}^{r-n,p}(f_i) & Z_{IBR}^{r-n,n}(f_i) \end{bmatrix} \\ \mathbf{Z}_{\mathbf{IBR}}^{\mathbf{CSD}}(f_b - f_i) &= conj\left(\begin{bmatrix} Z_{IBR}^{r-n,n}(f_i) & Z_{IBR}^{r-n,p}(f_i) \\ Z_{IBR}^{r-p,n}(f_i) & Z_{IBR}^{r-p,p}(f_i) \end{bmatrix}\right) \end{aligned} \quad (9)$$

The CSD impedance of the FSC-based WP extracted by both the proposed CSD-scan and the dq-to-CSD impedance transformation are compared in Fig. 5, the two models match well with each other which verifies (8) and (9).

C. CSD Impedance-Based Stability Analysis

The effectiveness of the proposed CSD-scan method is validated through IBSA using the FSC-based test system. The results are also verified by comparing with the dq- and sequence SISO-IBSA.

The open-loop transfer function of the dq-impedance-based model is defined as:

$$\mathbf{L}^{\mathbf{dq}}(f) = \mathbf{Z}_{\mathbf{Grid}}^{\mathbf{dq}}(f)\mathbf{Y}_{\mathbf{IBR}}^{\mathbf{dq}}(f) \tag{10}$$

where $\mathbf{Y}_{\mathbf{IBR}}^{\mathbf{dq}}$ and $\mathbf{Z}_{\mathbf{Grid}}^{\mathbf{dq}}$ are the dq-frame admittance and impedance of IBR and grid, respectively. $\mathbf{Y}_{\mathbf{IBR}}^{\mathbf{dq}}$ is extracted by EMT-level dq-scan, details can be found in [10]; $\mathbf{Z}_{\mathbf{Grid}}^{\mathbf{dq}}$ is extracted via the phasor solution-based scanning tool [21] and the sequence SISO to dq MIMO impedance transformation [13]. The positive sequence impedances of IBR $(Z_{IBR}^{p}(f_i))$ and grid $(Z_{Grid}^{p}(f_i))$ are extracted by EMT-level [5], [7] and phasor-solution-based p-scan methods, respectively.

The generalized Nyquist diagrams of $\mathbf{L}^{\mathbf{CSD}}(f)$ and $\mathbf{L}^{\mathbf{dq}}(f)$, and the Bode plots of $Z_{IBR}^{p}(f_i)$ and $Z_{Grid}^{p}(f_i)$ are shown in Fig. 6 and Fig. 7, respectively. The calculated resonance frequency (f_r) and phase margin (PM) by each method are listed in TABLE II. As shown in Fig. 6, the eigenvalue loci of $\mathbf{L}^{\mathbf{pn}}(f)$ and $\mathbf{L}^{\mathbf{dq}}(f)$ match well with each other with very small discrepancies, and both of them clockwise encircle the $(-1, j0)$ point, indicating an instability in the test system. It is worth noting that the eigenvalue loci of $\mathbf{L}^{\mathbf{CSD}}(f)$ consist of two identical curves with opposite directions: positive and negative sequence eigenvalues. The positive sequence (i.e., the first set of) eigenvalues should be used for identifying the f_r of the instability. The eigenvalue loci of $\mathbf{L}^{\mathbf{CSD}}(f)$ determines the unstable resonance at 108 Hz, with -0.5° PM; the eigenvalue loci of $\mathbf{L}^{\mathbf{dq}}(f)$ identifies the unstable resonance at 48 Hz in dq-frame (i.e., 108 Hz in SF), with -0.1° PM. The IBSA results of the two methods match well with the time domain EMT simulation in Fig. 3 verifying the accuracy of the CSD IBSA. There is only a 0.4° PM discrepancy between the CSD and dq IBSA results. Possible reasons for the discrepancy might be: i) errors induced during the admittance convergence in EMT-level frequency scanning procedures; ii) errors induced by the inverse operation of the IBR impedance/admittance matrices during data processing.

The sequence SISO IBSA fails to identify the instability and makes noticeable discrepancies on f_r due to the ignorance of the MFE. $|Z_{IBR}^{p}(f_i)|$ and $|Z_{Grid}^{p}(f_i)|$ in Fig. 7 have an intersection at 109.5 Hz, with 1.7° PM indicating a critical stable state rather than a critical unstable state. The sequence SISO IBSA might exhibit a larger errors if the IBR has a higher asymmetry between the d- and q- channel dynamics, which can be caused by using different inner-loop control parameters in d- and q- axes and larger PLL bandwidth, etc.

In summary, the accuracy of the CSD IBSA matches that of the dq IBSA and features a higher accuracy than the sequence SISO IBSA.

TABLE II
IBSA RESULTS OF THE SYSTEM UNDER STUDY

Item	csd-scan	dq-scan	p-scan
f_r (Hz)	108	108	109.5
PM	-0.5°	-0.1°	1.7°

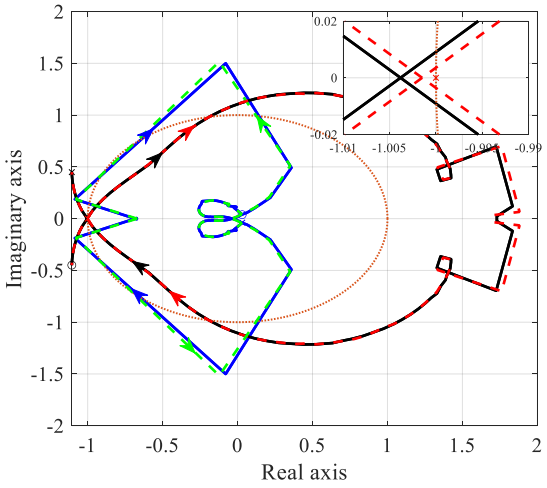

Fig. 6. The generalized Nyquist diagram of the CSD and dq IBSA. Blue and black solid lines: CSD impedance-based Nyquist plots; red and green dash lines: dq impedance-based Nyquist plots.

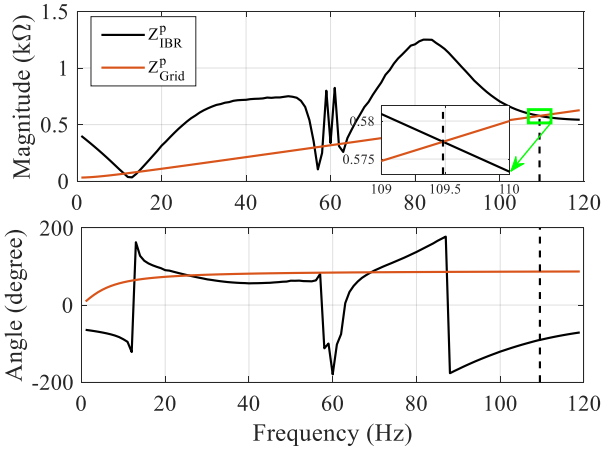

Fig. 7. Bode plot of the sequence SISO IBSA.

D. Computational Burden

The CSD-scan has a lower computational burden than the dq-scan as it requires no coordinate transformations for either the perturbation and the measurement signals, or the measured impedances/admittances. The amount of required scans is equal for the CSD- and dq-scan methods. Supposing the initialization time for the EMT-level frequency scanning is T_0, and the average convergence time of each frequency is ΔT, the theoretical total simulation time of the CSD- and dq-scans are

the same in SF:

$$t=\begin{cases} T_0+2n\Delta T, & 0<n<|\,f_b\,| \\ T_0+2\,|\,f_b\,|\,\Delta T, & f_b<n<|\,2f_b\,| \\ T_0+2\big(n-|\,f_b\,|\big)\Delta T, & n>|\,2f_b\,| \end{cases} \tag{11}$$

where $[1, n]$ Hz is the frequency scanning range, with 1 Hz frequency step. With the usage of impedance transformation, the CSD-scan in the frequency range between 1 Hz to $2f_b-1$ Hz can achieve the highest time efficiency, which is compatible with that of the p-scan method.

Compared with the sequence domain MIMO frequency scanning method in literature [15] and [20], the proposed CSD-scan method has a significantly lower computational burden because:

- In [15], [20], two sets of linear independent voltage vectors are used for perturbation, and the sequence coupled admittance matrix is calculated by:

$$\begin{bmatrix} Y_{p,p}(f_i) & Y_{p,n}(f_i) \\ Y_{n,p}(f_i) & Y_{n,n}(f_i) \end{bmatrix} = \begin{bmatrix} I^{p}_{(1)}(f_i) & I^{p}_{(2)}(f_i) \\ I^{n}_{(1)}(f_i-2f_b) & I^{n}_{(2)}(f_i-2f_b) \end{bmatrix} \cdot \begin{bmatrix} V^{p}_{(1)}(f_i) & V^{p}_{(2)}(f_i) \\ V^{n}_{(1)}(f_i-2f_b) & V^{n}_{(2)}(f_i-2f_b) \end{bmatrix}^{-1} \tag{12}$$

where subscripts of V and I indicate the first and the second set of the voltage perturbations and measured current vectors.

- The total simulation time of the method in [15], [20] can be represented as: $T_0+2n\Delta T,\quad n\geq 1$. Thus, in the frequency range of $[1, 2f_b-1]$, the total simulation time of the proposed CSD-scan method is only half of that in [15], [20].

The total simulation time of the CSD-scan (in the frequency range $[1, 59]\cup[61, 119]$ Hz) and dq-scan ($[1, 59]$ Hz in dq-frame) with 1 Hz frequency step are compared in TABLE III. The amplitude of perturbation is 0.01 p.u., the initialization time is 10 s, the forced running time is decreased to 1 s, and the convergence tolerance is 1%. As the dq impedance between 1-59 Hz corresponds to SF impedance between 1-119 Hz (exclude 60 Hz), dq- and CSD-scans in these two frequency ranges are equivalent. All simulations were performed on a desktop PC with the following specifications: CPU (Intel Core i5-7600 3.50GHz), 16 GB RAM, 64-bit operating system.

As seen in TABLE III, the simulation times of the CSD-scan and dq-scan methods are similar. On the other hand, CSD-scan does not require any additional simulation to differentiate the resonance and mirror frequencies.

TABLE III
SIMULATION TIME OF CSD- AND DQ-SCANS FOR FSC-BASED WP

$\lvert\mathbf{v}_{\mathbf{pabc}}\rvert$	Simulation time (s)	
	csd-scan (Hz)	dq-scan (Hz)
(p.u.)	$[1, 59]\cup[61, 119]$	$[1, 59]$
0.01	1983.9	1991.1

V. CONCLUSIONS

This paper proposed a new EMT-level CSD-scan method in SF to obtain the CSD impedance of IBR. The proposed method offers similar accuracy with dq-scan by accounting for the MFE. As the CSD-scan method is in SF, it has the following advantages over the dq-scan:

- It inherently differentiates the resonance and mirror frequencies, which is the major drawback in dq-scan method.
- Easy to implement compared to dq-scan as it does not require coordinates transformations of signals and impedances.
- The instability mechanism can be understood much easily by the engineers as the impedance values remain in SF.

Although CSD-scan has simulation speed advantage due to elimination of transformations, its impact is marginal in the considered system.

As CSD-scan method accounts for the MFE, it offers better accuracy compared to the p-scan.

VI. REFERENCES

[1] Y. Cheng et al. "Real-World Subsynchronous Oscillation Events in Power Grids with High Penetrations of Inverter-Based Resources," *IEEE Trans. Power Syst*., 2022.

[2] Cheng, Y., Huang, S. H. (Fred), Rose, J., Pappu, V. A., & Conto, J., "Subsynchronous resonance assessment for a large system with multiple series compensated transmission circuits," *IET Renewable Power Generation*. 13.1 : 27-32, 2019.

[3] L. Fan and Z. Miao, "An Explanation of Oscillations Due to Wind Power Plants Weak Grid Interconnection," *IEEE Trans. Sustain. Energy*, Vol. 9, No. 1, pp.488-490, 2018.

[4] L. Fan, C. Zhu, Z. Miao and M. Hu, "Modal Analysis of a DFIG-Based Wind Farm Interfaced With a Series Compensated Network," *IEEE Transactions on Energy Conversion*, 26.4, pp. 1010-1020, 2011.

[5] U. Karaagac, J. Mahseredjian, S. Jensen, R. Gagnon, M. Fecteau and I. Kocar, "Safe operation of DFIG based wind parks in series compensated systems," *IEEE Trans. Power Del*. 33.2 (2018): 709-718.

[6] M. Cespedes and J. Sun, "Impedance Modeling and Analysis of Grid-Connected Voltage-Source Converters," *IEEE Transactions on Power Electronics*, 29. 3 (2014): 1254-1261.

[7] B. Badrzadeh, M. Sahni, Y. Zhou, D. Muthumuni and A. Gole, "General methodology for analysis of sub-synchronous interaction in wind power plants, " *IEEE Transactions on Power Systems*, 28.2 (2013): 1858-1869.

[8] Y. Cheng, M. Sahni, D. Muthumuni and B. Badrzadeh, "Reactance Scan Crossover-Based Approach for Investigating SSCI Concerns for DFIG-Based Wind Turbines," *IEEE Trans. Power Deliv.*, vol. 28, no. 2, pp. 742-751, April 2013.

[9] B. Wen, D. Boroyevich, R. Burgos, P. Mattavelli and Z. Shen, "Small-Signal Stability Analysis of Three-Phase AC Systems in the Presence of Constant Power Loads Based on Measured d-q Frame Impedances," *IEEE Trans. Power Electron*. 30.10 (2015): 5952-5963.

[10] A. S. Trevisan, Â. Mendonça, R. Gagnon, J. Mahseredjian and M. Fecteau, "Analytically validated SSCI assessment technique for wind parks in series compensated grids," *IEEE Transactions on Power Systems* 36.1 (2021): 39-48.

[11] W. Ren and E. Larsen, "A Refined Frequency Scan Approach to Sub-Synchronous Control Interaction (SSCI) Study of Wind Farms," *IEEE Trans. Power Syst*. 31.5 (2016) 3904-3912.

[12] M. Kazem Bakhshizadeh et al., "Couplings in Phase Domain Impedance Modeling of Grid-Connected Converters," *IEEE Trans. Power Electron.*, vol. 31, no. 10, pp. 6792-6796, Oct. 2016.

[13] A. Rygg, M. Molinas,C. et. al., "A modified sequence domain impedance definition and its equivalence to the dq-domain impedance definition for the stability analysis of ac power electronic systems," *IEEE J. Emerg. Sel. Topics Power Electron.*, vol. 4, no. 4, pp. 1382–1396, Dec. 2016.

[14] X. Wang, L. Harnefors and F. Blaabjerg, "Unified Impedance Model of Grid-Connected Voltage-Source Converters," *IEEE Trans. Power Electron*. 33.2 (2018): 1775-1787.

[15] Y. Liao and X. Wang, "Stationary-Frame Complex-Valued Frequency-Domain Modeling of Three-Phase Power Converters," *IEEE Journal of*

Emerging and Selected Topics in Power Electronics 8.2 (2020): 1922-1933.

[16] N. Pogaku, M. Prodanovic and T. C. Green, "Modeling, Analysis and Testing of Autonomous Operation of an Inverter-Based Microgrid," *IEEE Trans. Power Electron*. 22. 2 (2007): 613-625.

[17] R. Middlebrook, "Input filter considerations in design and application of switching regulators," IEEE Ind. APPl. Soc. Annu. Meet. 1-6, 1997.

[18] N. Watson, J. Arrillaga, "Power Systems Electromagnetic Transients Simulation", 1st ed. London, UK: IET, 2003.

[19] U. Karaagac et al., "A generic EMT-type simulation model for wind parks with permanent magnet synchronous generator full size converter wind turbines," *IEEE Power Energy Technol. Syst. J*., vol. 6, no. 3, pp. 131-141, Sept. 2019.

[20] S. Shah, P. Koralewicz, V. Gevorgian and R. Wallen, "Sequence Impedance Measurement of Utility-Scale Wind Turbines and Inverters – Reference Frame, Frequency Coupling, and MIMO/SISO Forms," *IEEE Trans. Energy Convers*., vol. 37, no. 1, pp. 75-86, March 2022.

[21] B. L. Agrawal and R. G. Farmer, "Use of Frequency Scanning Techniques for Subsynchronous Resonance Analysis," *IEEE Trans. Power Appar. Syst.*, vol. PAS-98, no. 2, pp. 341-349, March 1979.

[22] A.G.J. MacFarlane and I. Postlethwaite, "The Generalized Nyquist Stability Criterion and Multivariable Root Loci," *International Journal of Control*, Vol. 25, pp. 81–127, 1977.

[23] J. Sun, "Impedance-Based Stability Criterion for Grid-Connected Inverters," *IEEE Trans. Power Electron*., Vol. 26, No. 11, pp. 3075-3078, 2011.